



Structural effects of nitrogen-doped titanium oxide supports on stabilization of ruthenium active species in carbon dioxide hydrogenation to formate

Kwangho Park^{a,1}, Kyung Rok Lee^{a,1}, Sunghye Ahn^{a,b}, Seong-Hoon Kim^c, Arsalan Haider^{a,b}, Seokhyun Choung^d, Jeong Woo Han^d, Kwang-Deog Jung^{a,b,*}

^a Clean Energy Research Center, Korea Institute of Science and Technology (KIST), 5, Hwarang-ro 14-gil, Seongbuk-gu, Seoul 02792, the Republic of Korea

^b Division of Energy & Environmental Technology, KIST School, Korea University of Science and Technology(UST), Seoul 02792, the Republic of Korea

^c R&D Center, Partek Corp, 49, Beolmal-ro 102gil, Donga-gu, Anyang-si, Gyeonggi-do 14065, the Republic of Korea

^d Department of Chemical Engineering, Pohang University of Science and Technology (POSTECH), Pohang, Gyeongbuk 37673, the Republic of Korea

ARTICLE INFO

Keywords:

CO₂ hydrogenation
Formic acid synthesis
Heterogeneous catalyst
H₂ storage
N-doped titanium oxide

ABSTRACT

A single atom Ru catalyst supported on a N-doped TiO₂ was investigated for the conversion of CO₂ to formate by hydrogenation. N-dopant sites induced a strong binding environment to Ru single-atom catalysts (SACs), resulting in a stable and atomically isolated dispersion state of Ru SACs upon metalation. Consequently, Ru/MN-TiO₂ exhibited enhanced catalytic stability, which incorporated both substitutional (N_s) and interstitial (N_i) dopant sites, retaining 42 % of its original relative activity after the fifth recycle test. In contrast, Ru/N-TiO₂, which contained only N_i-dopants, showed a lower stability, retaining only 19 % of its initial activity after the fifth run, and Ru/TiO₂ was fully deactivated after the third run. Density functional theory calculations revealed that the stronger binding ability of the N_s sites to the Ru species compared with that of the N_i sites and the bare surface of the TiO₂ structure improved the catalytic stability during hydrogenation.

1. Introduction

Green, high-energy-density, and cost-effective liquid organic hydrogen carriers (LOHCs) have been intensively explored for decades as a promising avenue for the bulk-scale storage and transportation of renewable energy [1–4]. Formic acid (FA), which is a product of CO₂ hydrogenation, shows promise as an LOHC because of its high gravimetric hydrogen capacity, corresponding to 53 g L⁻¹ and 4.4 wt%, and high volumetric energy density of 7.5 MJ L⁻¹ [5,6]. Furthermore, the chemical properties of FA, such as its relative non-toxicity and non-flammability, are critical advantages for safe and facile bulk-scale transportation. However, the technical readiness level for the utilization of FA as an LOHC has yet to be commercialized. Thus, intensive efforts have been made to develop efficient reversible catalytic systems for H₂ storage and release.

The dehydrogenation of FA, which is a hydrogen release reaction, is thermodynamically favorable with $\Delta G^\circ = -32.9 \text{ kJ mol}^{-1}$. However, it

is kinetically hampered, requiring catalyst systems for efficient conversion. Multiple catalyst systems have been intensively investigated to overcome this kinetic barrier and there have been several prominent studies that exhibit high catalytic activity, selectivity, and large-scale feasibility [7,8]. Conversely, the development of catalyst systems for H₂ storage, such as CO₂ hydrogenation to FA, is hindered because of the intricacy of the hydrogenation reaction. The conversion of gaseous CO₂ and H₂ to FA is thermodynamically unfavorable and requires aqueous conditions with base additives to generate a formate adduct [9,10]. Thus, FA separation units from the formate adduct should be integrated to afford pure FA. Moreover, the active metallic species that are detached in the product solution during the reaction can act as formate decomposition catalysts during the separation process. Therefore, the development of highly stable novel catalytic systems has been important for many years to increase the conversion efficiency of hydrogenation to a commercial scale [11,12].

Homogeneous catalysis has been an intensively studied field that has

* Corresponding author at: Clean Energy Research Center, Korea Institute of Science and Technology (KIST), 5, Hwarang-ro 14-gil, Seongbuk-gu, Seoul 02792, the Republic of Korea.

E-mail address: jkdcat@kist.re.kr (K.-D. Jung).

¹ These authors contributed equally to this work.

<https://doi.org/10.1016/j.apcatb.2023.122873>

Received 28 February 2023; Received in revised form 26 April 2023; Accepted 9 May 2023

Available online 10 May 2023

0926-3373/© 2023 The Authors. Published by Elsevier B.V. This is an open access article under the CC BY-NC-ND license (<http://creativecommons.org/licenses/by-nc-nd/4.0/>).

exhibited prominent catalytic activity and selectivity. However, because of the complexity of the catalyst separation process from the reaction medium, homogeneous catalysis is still lagging for commercialization [13,14]. Alternatively, heterogeneous catalyst systems have drawn interest because of their advantages, such as easy catalyst separation. However, they suffer from challenges such as low catalytic activity and deactivation behaviors, including metal leaching and agglomeration [15,16]. Therefore, we attempted to stabilize the metal components through the modulation of the support structures [17–19]. Recent studies have reported that heteroatom scaffolds, such as N atoms incorporated on the surface of the catalyst support, significantly increase the binding strength of the active metal species to the catalyst support by retaining the atomic level of dispersion, that is, single-atom catalysts (SACs) [20–25].

For decades, supported Ru SACs have been extensively studied, demonstrating significant advancements in catalytic performance [26–31]. In our previous reports, the significantly enhanced stability of Ru SACs supported on N-rich support materials, such as covalent triazine frameworks and N-doped carbons, was demonstrated for CO₂ hydrogenation to formate from long-term stability tests over continuous operations [32–36]. However, N-incorporated carbon support materials are expensive, mechanically fragile, and difficult to handle for practical use owing to the hydrophobic nature of the surface. Therefore, although conventional metal oxides, such as TiO₂ and SiO₂, show much lower catalytic performance, various approaches have been attempted to introduce functional groups, including heteroatoms, into metal oxide materials to overcome the low catalytic performance of metal oxide-supported catalysts [37,38]. However, the complex procedures for the synthetic steps limit their use on a large scale and the elucidation of the underlying principles for the stabilization effect of the support on the metal components has rarely been reported.

N-doping of TiO₂ has been widely exploited in photocatalytic fields. Thus, it is a well-reported method to control the electronic properties of TiO₂, which is facilitated by the similar atomic sizes of N and O in the lattice structure, resulting in substitutional N (N_s)- and interstitial N (N_i)-dopant sites [39–41]. Along with its intrinsic characteristics, such as high thermal and chemical stabilities, non-toxicity, and low manufacturing cost, N-doped TiO₂ is a relevant catalyst support material for various chemical reactions [42–46]. Recently, it has been reported that catalytic performance can be enhanced by rationally tuning the interaction between the supported metal catalysts and N-doped TiO₂ materials. Ao et al. reported that the electronic nature of supported Pd catalysts can be tuned by changing the chemical properties of N-doped TiO₂ materials for H₂O₂ synthesis [44]. Chen et al. demonstrated that N-scaffolds on TiO₂ effectively improved the dispersity and stability of Pd nanoparticles (NPs) for the hydrogenation of nitrobenzene to aniline [45]. Yan et al. reported Ru SAC and Ru NP catalysts supported on amine-functionalized MOF-derived N-doped TiO₂/C supports that exhibited improved catalytic activity for electrocatalytic and photocatalytic hydrogen evolution reactions. In this study, the initial loading amount of Ru during the synthesis procedure significantly influenced both the final morphology and chemical state of the catalyst supports and the dispersion state of the Ru species [46]. However, the underlying principle of the stabilization effect of N-dopant sites according to the chemical states of the metal catalysts has not yet been explicitly revealed and the investigation of this principle for CO₂ hydrogenation is of great importance.

This study reports the synthesis of N-doped TiO₂ supports prepared via the co-calcination of melamine and Ti(OH)₄ powder (MN-TiO₂). The structure and chemical states of the N-dopant sites on the prepared support materials varied by using different synthesis method, endowing the different binding environments of the metal catalysts. Upon Ru metalation, it was confirmed that the Ru species were bound to the N sites and maintained an isolated dispersion state on the support. To validate the underlying role of the N-dopant sites in improving the catalytic performance, hydrogenation of CO₂ to formate was

investigated using a batch reactor and the results were compared with Ru catalysts supported on N-TiO₂, which were prepared using a conventional method, and bare-TiO₂. Finally, density functional theory (DFT) calculations were conducted to verify the electronic interaction between the Ru atoms and N-dopant sites with different chemical states incorporated on the TiO₂ structure and the results were compared to that of the bare TiO₂ support.

2. Experimental section

2.1. Materials

Titanium isopropoxide (TTIP, 99 %), melamine (99 %), triethylamine (Et₃N, 99 %), titanium oxide (TiO₂, anatase), and RuCl₃·xH₂O were purchased from Sigma-Aldrich Co. An ammonia solution (28–30 %) was purchased from Samchun Co. (Republic of Korea). An anhydrous methyl alcohol solution was supplied by Daejung Co. (Republic of Korea). Liquid CO₂ (99.999 %) and H₂ (99.999 %) were supplied from Sinyang Gas Industries (Republic of Korea).

2.2. Preparation of the support materials: MN-TiO₂, N-TiO₂ and TiO₂

The N-doped TiO₂ prepared by melamine and Ti precursor, MN-TiO₂, supports were synthesized using TTIP, which was dissolved in a 28 % of aqueous ammonia solution (50 mL) and stirred at 25 °C for 1 h. Thereafter, the precipitate was filtered with water (150 mL) and ethanol (150 mL) and dried under vacuum at 80 °C for 6 h. Dried Ti(OH)₄ (1 g) was ground and mixed with melamine (2 g) and calcined in a tube furnace for 4 h at a heating rate of 1 °C min^{−1} under a nitrogen atmosphere. N-TiO₂ was prepared by calcining a mixture of commercially purchased TiO₂ (1 g) and melamine (2 g) at 550 °C for 4 h in a tube furnace at a heating rate of 1 °C min^{−1} under a nitrogen atmosphere. The purchased anatase TiO₂ was used as a [supporting material](#) for comparisons without further purification.

2.3. Preparation of Ru/MN-TiO₂, Ru/N-TiO₂, and Ru/TiO₂ catalysts

The as-prepared support material (500 mg) was dispersed in methanol (50 mL) and ultrasonicated for 10 min. Thereafter, a methanolic solution of RuCl₃·xH₂O (20 mg dissolved in 30 mL) was added to the aforementioned mixture and sonicated for 10 min. After sonication, the suspension was stirred under reflux for 24 h. Subsequently, the mixture was cooled to room temperature, filtered, and washed several times with methanol. The resulting black powder was dried under vacuum at 60 °C for 24 h.

2.4. Characterizations

Transmission electron microscopy (TEM) images and energy-dispersive spectroscopy (EDS) mapping were analyzed using a TEM-Talos (F200X) operating at an accelerating voltage of 200 kV with a LaB₆ source. Ru nanocluster images were obtained by scanning transmission electron microscopy using a double Cs-corrected Titan Themis TEM (FEI; TitanTM 80–300). X-ray diffraction (XRD) was performed on a diffractometer (M/S, Shimadzu Instruments, Japan) using Ni-filtered Cu K α radiation (λ = 0.15418 nm). The operating voltage was 40 kV and the current was 30 mA at a scanning rate of 1 °C min^{−1}. X-ray photoelectron spectroscopy (XPS) was performed on the catalysts on a PHI 5000 Versa Probe spectrometer (Ulvac-PHI, Japan) with a monochromatized Al K α (1486.6 eV) excitation source operated at 15 kV and 25 W. The X-ray absorption spectroscopy measurements to collect the near edge X-ray absorption fine structure (NEXAFS) and X-ray absorption fine structure (XAFS) spectra were conducted using 10D XAS Korea Institute of Science and Technology, 8 C Nano XAFS and 10 C Wide XAFS beamline in the Pohang Accelerator Laboratory (PLS-II, 3.0 GeV, South Korea), respectively. High-performance liquid chromatography (HPLC)

was performed using a YL 9100 Plus HPLC system (YL Instruments Co. Ltd., South Korea) with a refractive index detector and an Aminex HPX-87 H column. The column was operated at 50 °C and an eluent (5 mM H₂SO₄ solution) was used at a flow rate of 0.6 mL/min. The samples were pre-treated with an inductive coupled plasma optical emission spectroscopy (ICP-OES) sample preparation system I (Ethos 1). The atomic weight percentage of Ru was measured using an Avio 500 ICP-OES analyzer (PerkinElmer, USA). ¹³C nuclear magnetic resonance (¹³C NMR) spectra were obtained with a Bruker Ascend 400 MHz. Gas chromatography (GC) was analysed by YL-6500 (Younglin, Rep. of Korea) equipped with a thermal conductivity detectors, and a Restek shincarbon ST 100/120 column using Ar as a carrier gas. Carbon monoxide (CO) adsorption investigations were conducted utilizing a Nicolet iS 10 Fourier Transform Infrared Spectrometer, equipped with a Mercury Cadmium Telluride (MCT) detector (Thermo Fisher Scientific), in conjunction with an in situ diffuse reflectance infrared fourier transform spectroscopy (DRIFTS) apparatus (Spectra-tech). The spectral data were acquired by obtaining 128 scans at a resolution of 4 cm⁻¹, employing a transmittance mode of operation. Prior to acquiring the background measurements, the samples underwent an Argon (Ar) drying process for a duration of 30 min at a temperature of 150 °C. Following this, a 5 % CO/Ar mixture was introduced into the chamber at ambient temperature, maintaining a flow rate of 20 mL/min. Upon reaching CO saturation, a subsequent Argon purge was initiated with an identical flow rate of 20 mL/min, continuing until the complete absence of gaseous CO was confirmed. As a control experiment, Ru/TiO₂ catalyst was reduced with a 50 mL/min of 10 % H₂/Ar at 500 °C for 4 h and then the CO-DRIFTS was performed under the same procedure.

2.5. Procedure for CO₂ hydrogenation to formate

The catalytic performance of the prepared catalysts was evaluated in a batch reactor. In general, a catalyst (60 mg) and a 3 M aqueous solution of Et₃N (40 mL) were used. After pressurizing with CO₂ and H₂ with a total pressure of 8 MPa (CO₂/H₂ = 1) at 25 °C, the reaction was conducted at 120 °C with stirring at 500 rpm. The pressure was increased to 11.6 MPa at the reaction temperature. Afterward, the suspended catalyst was collected and filtered through a 0.2 μm filter paper. The formate concentration was determined by HPLC analysis using the filtrate solution. The stability of the catalysts was examined in the CO₂ hydrogenation reaction over three successive runs using 60 mg of the catalyst in 40 mL of a 3 M aqueous Et₃N solution under the same conditions as mentioned above. After the recyclability test, the catalyst was recovered by filtration, washed with water (200 mL), and dried under vacuum at 60 °C for 18 h before reuse. The remaining Ru content in the recovered catalyst after each run was estimated by subtracting the amount of leached Ru in the filtrate, which was determined by ICP-OES analysis, from the initial Ru content.

2.6. Density functional theory calculations for structural modeling of representative catalytic active sites

DFT calculations were conducted using the Vienna ab initio simulation package (VASP 6.2.0) to investigate the catalytic phenomena of Ru SACs supported on N-TiO₂. The projector-augmented wave method was used to express the interaction between the ions and core electrons. The generalized gradient approximation with the Perdew–Burr–Ernzerhof functional was used to describe the electron exchange–correlation energy. The kinetic energy cut-off for the plane wave was set to 400 eV and the total energy of all the systems converged when the energy was less than 0.2 meV. A 3 × 4 × 1 Monkhorst–Pack grid was selected for k-space integration. Ionic relaxation in a fixed volume was performed with a convergence criterion of 0.03 eV Å⁻¹. The vacuum layer along the z-direction was 20 Å to avoid interference from the bottom layer in the upper cell. The Bader charges were calculated using the Henkelman algorithm. The adsorption energy of RuCl₃ on each TiO₂

surface, E_{abs}, was calculated as follows:

$$E_{\text{abs}} = E_{\text{RuCl}_3\text{-surface}} - E_{\text{RuCl}_3} - E_{\text{surface}},$$

where E_{RuCl₃-surface}, E_{RuCl₃}, and E_{surface} are the total energies of the adsorbed RuCl₃ and RuCl₃ molecules in the vacuum cell and the clean surface, respectively.

3. Results and discussion

3.1. Characterization of prepared support materials

To optimize the preparation method, the synthesis of MN-TiO₂ support was initially conducted using the grind-mixed powder of Ti(OH)₄ and melamine as a nitrogen source at different calcination temperatures of 500, 550, 600, and 650 °C. X-ray diffraction (XRD) was performed in order to trace the structural change of as-prepared samples at different thermal conditions. As shown in the Fig. S1, the diffraction pattern for the sample prepared at 500 °C showed a peak of the (101) plane of anatase-TiO₂ at 2θ = 24° with low intensity and broad shape and an intense peak of the (002) plane of g-C₃N₄ at 2θ = 28°. Compared to the XRD pattern of the Ti(OH)₄ precursor that did not display any crystalline phase, this result indicates the initial stage for the growth of TiO₂ lattices with a predominance of the g-C₃N₄ structure. Meanwhile, Fig. 1 showed that the prepared sample calcined at 550 °C exhibited the characteristic peak of anatase TiO₂, whereas the peak of g-C₃N₄ noticeably disappeared in the diffraction pattern with the emergence of the peak at 2θ = 43°. This is attributed to the thermal decomposition of g-C₃N₄ over 550 °C and the simultaneous N doping steps on the Ti-O structure, generating the (200) plane of Ti-N lattices on the surface structure [47]. Then, the diffraction pattern of Ti-N structure completely disappeared over the calcination temperature of 600 °C due to the excessive thermal decomposition, which remained anatase TiO₂ and rutile TiO₂ structure. Thus, the calcination temperature of 550 °C was chosen as the optimal condition for the preparation of MN-TiO₂ support, in which the simultaneous N-doping by the thermal decomposition of g-C₃N₄ and TiO₂ crystal growth effectively occurred. For comparison, a support material was also prepared by calcining the mixture of pristine anatase TiO₂ and melamine at 550 °C, which was labeled as N-TiO₂, but in this case, the crystalline phase of Ti-N was not confirmed.

XPS was performed to investigate the compositional changes and chemical states of the components on the surface of the prepared support samples (Fig. 2a–d). The survey spectrum of MN-TiO₂ showed a low intensity of the C 1s and N 1s peaks (Fig. S2a). As shown in the deconvoluted C 1s spectra of MN-TiO₂ (Fig. 2a), the characteristic peak of

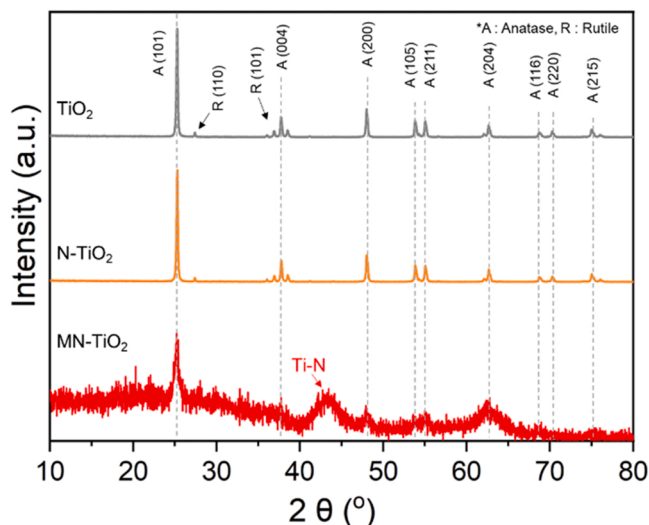


Fig. 1. XRD patterns of pristine TiO₂ and N-doped TiO₂.

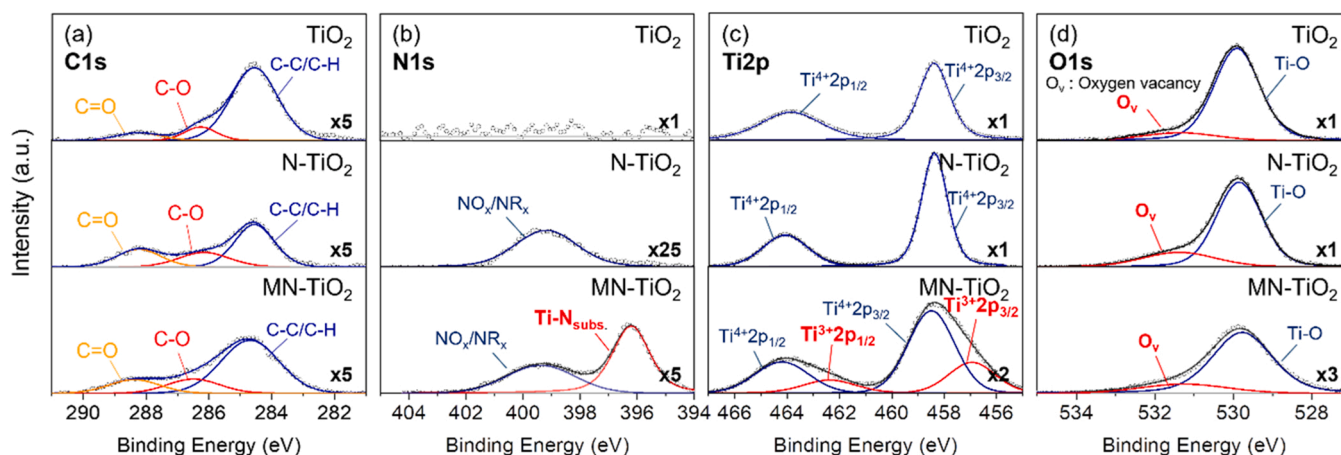


Fig. 2. Deconvoluted XPS spectra at (a) C 1s, (b) N 1s, (c) Ti 2p, and (d) O 1s in prepared support materials.

C–N = C at 288.0 eV is absent, indicating the thermal decomposition of g-C₃N₄ occurred at the calcination temperature of 550 °C. Also, Fig. 2b showed that the peak of pyridinic N at 398.6 eV was not observed in the deconvoluted N 1s spectra of MN-TiO₂, supporting the complete decomposition of g-C₃N₄ structure. The N 1s spectra of MN-TiO₂ were deconvoluted in two states. As stated in previous reports, the deconvoluted N 1s peak at 396.2 eV was assigned to the N_s-dopant species located at the O sites in the TiO₂ lattice structure [48–51]. Further, another peak at 399.4 eV was widely considered as N_i species derived from embedded substances, such as NO_x and NR_x. In contrast to the MN-TiO₂, the N-TiO₂ sample has only one peak at 399.4 eV, which verifies that post-synthetic melamine treatment with TiO₂ cannot generate N_s sites [50,51].

In the Ti 2p spectra (Fig. 2c), the MN-TiO₂ shows two chemical states at 458.5 (Ti⁴⁺) and 456.9 eV (Ti³⁺), whereas the other samples show only the Ti⁴⁺ peak. Additionally, the O 1s spectra show two peaks at 529.8 and 531.3 eV for the Ti–O species and oxygen vacancy (O_v), respectively (Fig. 2d). These results reveal that defect sites on the MN-TiO₂ support are generated owing to the formation of the Ti–N structure under N-doping conditions, which typically occurs because of the electronic compensation effects of the electronegativity difference between the O atoms and N_s-dopants [48,49].

Synchrotron-based NEXAFS was performed using soft X-rays to confirm the local atomic structure of the N, Ti, and O atoms in TiO₂ and N-doped TiO₂. The N K-edge NEXAFS spectra of MN-TiO₂ shows two sharp peaks at 397 and 402 eV and one broad peak at 409.5 eV (Fig. 3a). The two sharp peaks are attributed to the t_{2g} and e_g resonance peaks, which originate from the electronic transition to the N 2p π -Ti 3d and N 2p σ -Ti 3d orbitals. The broad peak in a high energy range is attributed to the electronic transition to the N 2p–Ti 4sp antibonding state [52,53]. From the N K-edge of MN-TiO₂ (Fig. 3a, red line), it is deduced that N_s-dopant sites can be generated in the octahedral coordination of the

anatase TiO₂ structure evolved through Ti(OH)₄ and melamine. In contrast, only two resonance peaks with very low intensities are identified at 401 and 403 eV in the N K-edge spectra of N-TiO₂, corresponding to N–H and N–O bonds derived from interstitial N species. These results suggest that only N_i-dopant can be generated in anatase TiO₂ evolved through physically mixed anatase TiO₂ and melamine from the N K-edge (Fig. 3a, blue line). Fig. 3b shows the NEXAFS spectra at the Ti L-edge of the prepared TiO₂ specimens, which have four distinct absorption peaks. The two peaks at low energies are derived from the electronic transition at the L₃-edge (2p_{3/2} → 3p_{5/2}), while the other two peaks originate from the transition at the L₂-edge (2p_{1/2} → 3p_{3/2}) [53, 54]. The absorption peaks at the L₃- and L₂-edges are divided into two peaks because of the d-orbital splitting into two groups, namely t_{2g} (d_{xy}, d_{yz}, and d_{xz}) and e_g (d_{z²} and d_{x²-y²}). The spectra of TiO₂ and N-TiO₂ exhibit the typical peaks of the anatase structure, whereas the Ti L-edge of the MN-TiO₂ exhibits a broad L₃-e_g peak and the L₂-e_g peak shifts to the low-energy state. Additionally, a pre-edge is observed at 457 eV, indicating that O_v is generated in the MN-TiO₂ structure during the N-doping process. These spectra indicate that the MN-TiO₂ catalyst has a distorted structure of the original octahedral coordination of the anatase structure, caused by the generation of N_s-dopant sites [52,53]. The O K-edge spectrum exhibits strong resonance peaks of t_{2g} and e_g (Fig. 3c), which result from the electronic transition from O 2p to the Ti 3d hybridized orbital in the octahedral coordination [54]. The peak shape of MN-TiO₂ is broader than those of TiO₂ and N-TiO₂, indicating weakened Ti–O interactions from the distorted octahedral structure. In the photon energy range above 536 eV, the peak at 547 eV can be attributed to the electron transition from O 1s to the O 2p/Ti 4sp and 4p hybridized orbitals, and the peak at 540 eV can be attributed to the electron transition from O 1s to O 2p. In contrast to TiO₂ and N-TiO₂, the two peaks at 540 and 547 eV of MN-TiO₂ become so broad that they can no longer be distinguished, indicating the low crystallinity and lack of long-range

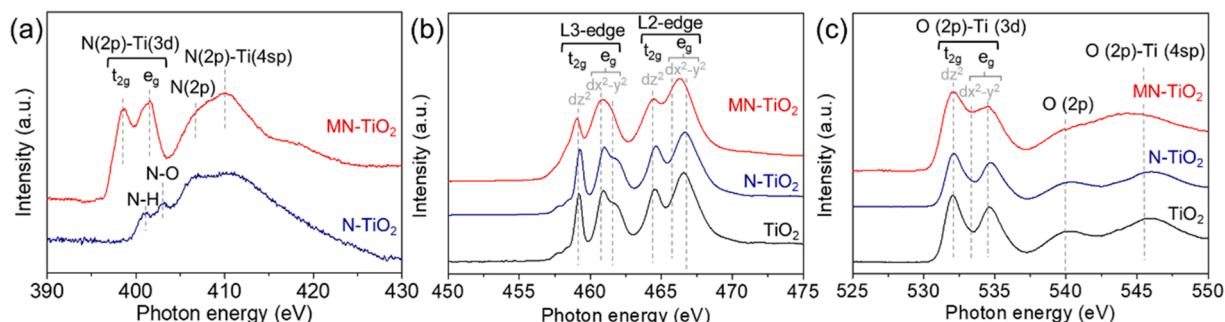


Fig. 3. NEXAFS spectra of (a) N K-, (b) Ti L-, and (c) O L-edges for prepared supports.

order in the crystalline TiO_2 structure [52,53].

3.2. Characterization of Ru single atom catalysts supported on the pristine and N-doped TiO_2

The chemical states of the atomic components of the prepared Ru catalysts were further investigated by NEXAFS, XPS, XAFS, and TEM to confirm the changes in the structural and electronic properties during Ru immobilization. Fig. 4a, b, and c show the N K-, Ti L-, and O L-edge results, respectively, after Ru immobilization. Upon Ru metalation on the prepared supports, the t_{2g} and e_g resonance peaks at 397 and 402 eV in the N K-edge spectrum of MN-TiO₂ diminish markedly and the peak at 410 eV broadens (Fig. 4a). In contrast, there is a slight decrease in the intensity of the two peaks assigned to the N-H and N-O bonds of the N_i species. However, no difference between the Ru metalated catalysts and supports is observed in the spectra at the Ti L- and O K-edge results (Fig. 4b and c). This indicates that the local coordination environment of the N sites is considerably changed by Ru immobilization. However, Ti and O are not associated with Ru metal binding.

The binding energy of Ru 3d for all samples is observed at 281.7 eV, indicating that the Ru components retained their original oxidation state of 3 + (Fig. 4d) [55]. Similar to the NEXAFS spectra, no changes are observed in the XPS spectra of the N and Ti components of Ru/TiO₂ and

Ru/N-TiO₂ (Fig. 4f, S4, and S5). However, in Fig. 4e for the N 1s spectrum of Ru/MN-TiO₂, the intensity of the deconvoluted Ti-N peak at 396.2 eV is notably diminished after Ru immobilization, which indicates charge transfer by the coordination of the Ru metal and N_s-dopants in the support. Moreover, the deconvoluted peak of Ti³⁺ in the Ti 2p XPS spectrum at 457 eV is significantly diminished for Ru/MN-TiO₂, while that of the O_v defects in the O 1s XPS spectrum at 531 eV is retained (Fig. S3). This indicates a change in the electronic properties of the catalyst due to charge transfer between the Ru and N scaffolds on the support in the presence of the immobilized Ru species.

Ru K-edge X-ray absorption spectroscopy was used to further confirm the electronic and structural properties of the Ru species in the Ru catalysts. The X-ray absorption near-edge structure spectra shown in Fig. 4g exhibit that the energy absorption threshold for Ru/MN-TiO₂ is lower than for RuO₂, but higher than for Ru foil, and is similar to that of RuCl₃. This result demonstrates that the oxidation state of the supported Ru species is similar to that of Ru³⁺. The extended X-ray absorption fine structure spectra for Ru are shown in Fig. 4h. Ru radial distances of Ru-Ru, Ru-O, and Ru-Cl are estimated to be 2.5, 1.6, and 1.9 Å, respectively, which are equivalent to that of the Ru foil (2.5 Å), RuO₂ (1.6 Å), and RuCl₃ (2.0 Å) in Fig. 4h. The Ru radial distances of Ru/TiO₂ (2.0 Å) and Ru/N-TiO₂ (1.8 Å) are similar to those of Ru-Cl (1.9 Å), indicating that Ru-Cl is the major Ru species on TiO₂ and N-TiO₂.

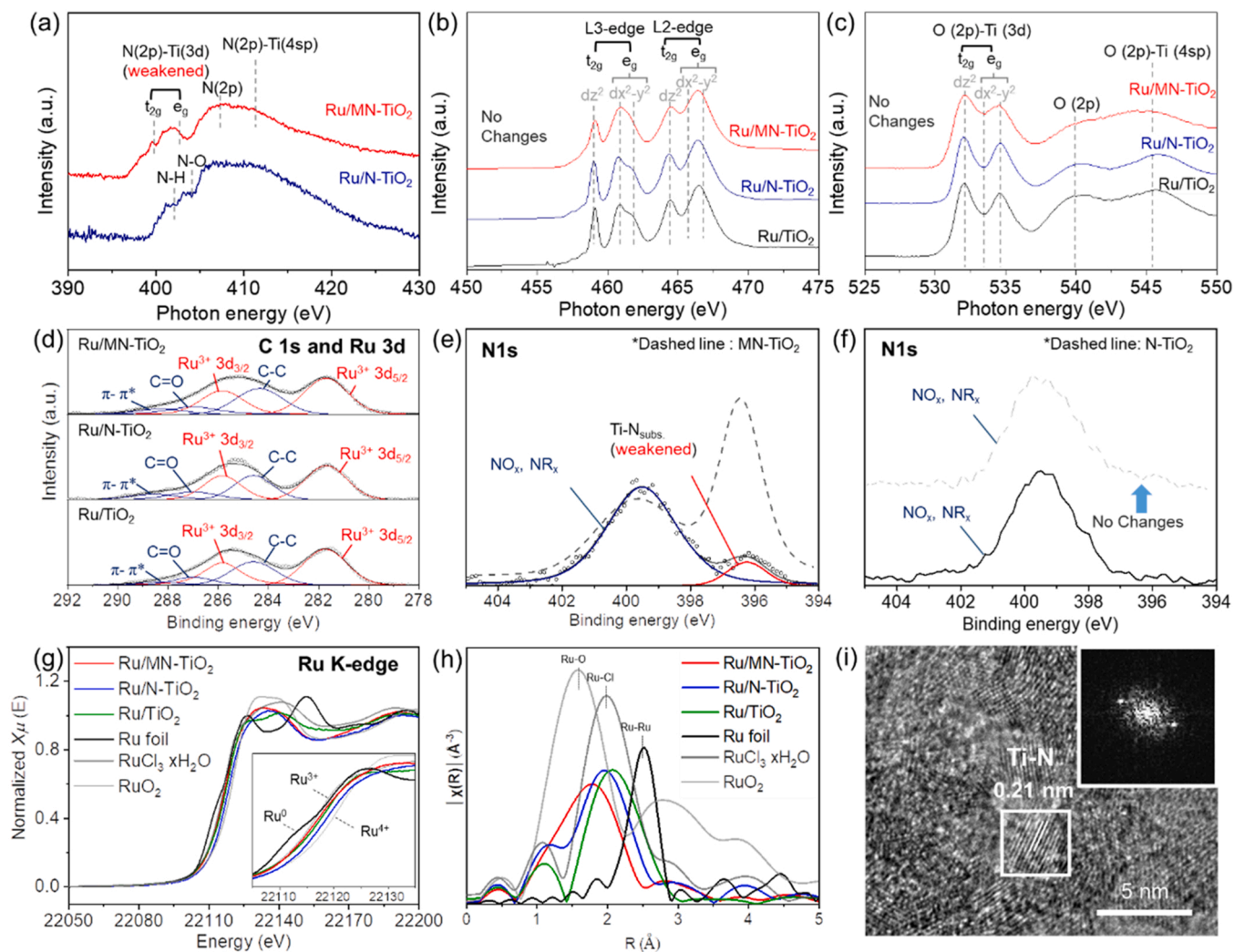


Fig. 4. Characterization of supported Ru catalysts. NEXAFS spectra of (a) N K-, (b) Ti L-, and (c) O L-edges for supported Ru catalysts. (d) Deconvoluted Ru 3d XPS spectra of Ru/MN-TiO₂, Ru/N-TiO₂, and Ru/TiO₂. Deconvoluted N 1s XPS spectra of (e) Ru/MN-TiO₂ and (f) Ru/N-TiO₂. (g) Ru K-edge X-ray absorption near-edge structure, (h) Extended X-ray absorption fine structure spectra of Ru/MN-TiO₂, Ru/N-TiO₂, Ru/TiO₂, and reference materials, and (i) HR-TEM image and Fast Fourier transform pattern (inset) of Ru/MN-TiO₂.

However, Ru/MN-TiO₂ has a bond length of approximately 1.7 Å with a broad shape, which is derived from the merged peak of Ru–N and Ru–Cl coordination. Furthermore, the metallic Ru–Ru scattering peak of each supported Ru catalyst is not clearly observed, indicating that the Ru species are atomically dispersed on the support material.

To obtain additional evidence for the single atomic state of Ru species, CO adsorption studies using DRIFTS were conducted on the synthesized catalysts (Fig. S6). As a result, we successfully gathered analysis data for the Ru/TiO₂ catalyst. The findings obtained after CO adsorption and subsequent Ar purging exhibited two vibrational frequencies at 2020 cm^{−1} and 2078 cm^{−1}. Based on the XPS and XAS analysis outcomes, these frequencies can be assigned to Ru–CO (monodentate) and Ru³⁺–(CO)_x (geminal coordination), respectively. Conversely, the control catalyst, Ru/TiO₂-H₂-500, which was reduced under an H₂ atmosphere at 500 °C, displayed a prominent and broad vibrational frequency at 1960 cm^{−1} (Fig. S7). This observation can be attributed to the CO species in bridged coordination on the surface of Ru nanoparticles. Our observations align with those reported in other studies [56–58]. Importantly, the absence of bridged CO, indicative of Ru nanoparticles, confirms the single atomic state of Ru species. Unfortunately, we encountered difficulties in obtaining clear analysis data for the Ru/N-TiO₂ and Ru/MN-TiO₂ catalyst. This emerged due to the extremely weak IR signal for CO bound to Ru species ascribed to the black color of the support materials, which results in the absorption of scattered IR beams by the support material.

High-resolution TEM was performed to identify the morphology of the catalysts and dispersion state of the supported Ru species (Fig. 4i). As shown in Fig. 4i, a polycrystalline morphology of MN-TiO₂ is observed with grain sizes of approximately 10 nm. Fast Fourier transform (FFT) was performed to study the crystalline structure on the surface (Fig. 4i, inset). The obtained patterns by the FFT analysis show the presence of the Ti–N structure by confirming the lattice distance of 0.21 nm, which is also observed in the results of the XRD analyses. Meanwhile, the TEM image reveals the absence of Ru NPs and the EDS mapping image displays a homogeneous distribution of Ru atoms throughout the support material, indicating the successful immobilization of Ru species and inhibition of agglomeration into the Ru NPs (Figs. S8 and S9). However, the dispersion state of Ru species at the atomic level could not be distinguished even by high-angle annular dark-field scanning TEM analysis because of the low Z-contrast between Ru and Ti (Fig. S10).

3.3. Catalytic performance of Ru single atom catalysts supported on the pristine and N-doped TiO₂

An evaluation of the initial catalytic activity of the prepared Ru catalysts was performed for hydrogenation under 8 MPa (CO₂:H₂ = 1:1, at 25 °C) and 120 °C for 2 h in a batch reactor and the physicochemical properties and catalytic activities of the prepared catalysts are listed in Table 1. The Brunauer-Emmett-Teller surface areas (S_{BET}) and mean pore diameters of the prepared catalysts were determined using N₂ isotherm adsorption-desorption analyses. According to Table 1, the pristine anatase-based TiO₂-supported catalysts (Ru/TiO₂ and Ru/N-TiO₂) exhibited much higher S_{BET} values than the area of the Ru/MN-TiO₂ catalysts. The activities of the prepared catalysts are also listed in Table 1. The TON and TOF values listed in Table 1 were obtained from the reaction for 2 h. It's worth noting that in the preliminary test for hydrogenation, using RuCl₃·xH₂O with a comparable amount of Ru to that of the charged as-prepared catalysts, a TON of 400 was achieved over a period of 2 h. The Ru/MN-TiO₂ catalyst displayed the highest TOF value among the prepared Ru catalysts at 1590 h^{−1}, making it the most effective among the supported catalysts. The catalytic activity of Ru/MN-TiO₂ is comparable to other Ru SAC based heterogeneous catalysts in the literature (Table S2). On the other hand, the Ru/TiO₂ catalyst with the highest S_{BET} had the lowest catalytic activity, only twice that of unsupported RuCl₃·xH₂O. Comparing the catalytic activities of Ru/N-TiO₂ (S_{BET}: 102.5 m²·g^{−1}) and Ru/MN-TiO₂ catalyst

Table 1

Physico-chemical properties and catalytic activity of prepared catalysts.^a

Sample	S _{BET} (m ² g ^{−1})	d _{mean} (nm)	Ru content ^b (wt%)	[FA] ^c (mol L ^{−1})	TON ^d	TOF ^e (h ^{−1})
RuCl ₃ ·xH ₂ O ^f	–	–	–	0.080	400 ^f	200
Ru/MN-TiO ₂	67.1	8.7	1.35	0.638	3180	1590
Ru/N-TiO ₂	102.5	7.5	1.25	0.568	3060	1530
Ru/TiO ₂	120.3	4.3	1.16	0.071	820	410

^a A typical reaction was carried out using 60 mg of the catalyst in 40 mL of a 3 M aqueous Et₃N solution for 2 h with a stirring rate of 500 rpm. The initial pressure was increased to 8.0 MPa at 25 °C with H₂/CO₂ = 1:1, which increased to 11.6 MPa at 393 K.

^b Ru content was determined using ICP-OES analysis.

^c The concentration of formate was determined using high-performance liquid chromatography.

^d TON = mole_{FA}/mole_{Ru}.

^e TOF = TON/reaction time.

^f Hydrogenation was conducted using 1.65 mg of a RuCl₃·xH₂O precursor.

(S_{BET}: 67.1 m²·g^{−1}), it is apparent that the Ti–N structure is crucial to the catalytic activity of TiO₂-based Ru catalysts. In the batch process, Ru/MN-TiO₂ selectively catalyzed the conversion of CO₂ to formate, exhibiting nearly 100 % selectivity. No side products, including CO, CH₄, CH₃OH and carbamate were detected as evidenced by GC and ¹³C NMR analyses (Fig. S11 and S12). In particular, the catalyst poorly catalyzed the CO₂ hydrogenation reaction when conducted separately under pure water and neat Et₃N conditions (Table S3). This implies that water and Et₃N play a crucial role in forming bicarbonate during the reaction and stabilizing the generated formate. These findings are consistent with the results of reaction mechanism studies, based on which a plausible mechanism has been suggested (Fig. S14) [28,33].

To evaluate the recyclability of Ru/MN-TiO₂, Ru/N-TiO₂, and Ru/TiO₂ catalysts, a series of five recycling tests for CO₂ hydrogenation were conducted under standard conditions, as illustrated in Fig. 5 and Table S4. During the recycling tests, the catalyst was recovered via filtration, washed, and dried under a vacuum before re-use. To account for potential catalyst losses during the recovery steps, the specific activity, measured as the number of formate molecules produced per recovered weight of the catalyst (mmol_{FA}/g_{cat}), was utilized to evaluate the activity change of each cycle. The relative specific activity of each cycle was subsequently calculated as a percentage of the specific activity obtained in the first cycle. The Ru/TiO₂ catalyst exhibited some initial

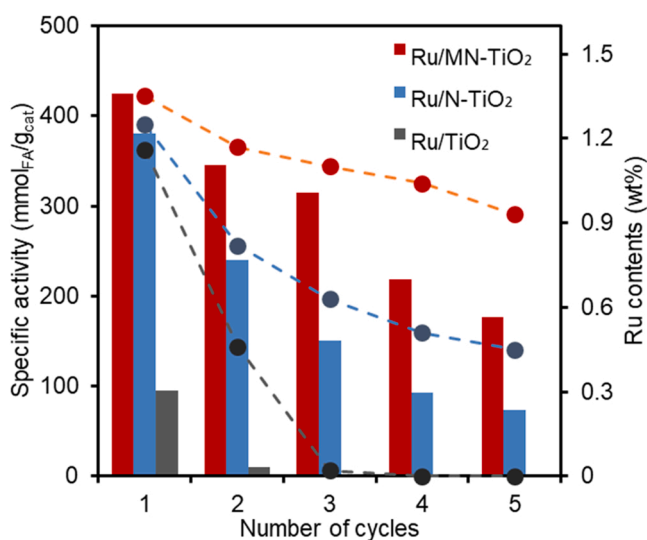


Fig. 5. Specific catalytic activity (column) and estimated Ru content (dot and line) of Ru/MN-TiO₂, Ru/N-TiO₂, and Ru/TiO₂ for recycle tests.

catalytic activity, with an initial specific activity of 95 mmol_{FA}/g_{cat}, but was significantly deactivated, recording only 10 mmol_{FA}/g_{cat} of specific activity, equivalent to 11 % of its initial activity, after the second cycle, and was fully deactivated after the third cycle (Fig. 5, gray column and Table S4). In contrast, Ru/N-TiO₂ showed relatively high stability, retaining 73 mmol_{FA}/g_{cat} of specific activity, corresponding to 19 % of its initial specific activity, after the fifth cycle (Fig. 5, blue column and Table S4). On the other hand, Ru/MN-TiO₂ displayed excellent stability, maintaining a promising 177 mmol_{FA}/g_{cat} of specific activity, equivalent to 42 % of its initial specific activity, after the fifth cycle (Fig. 5, red column and Table S4). Fig. S16 illustrates the gradual increase in TON value over a 30-hour period for the CO₂ to formate conversion reaction using Ru/MN-TiO₂ catalyst. The reaction attained an equilibrium at an acid to amine ratio of 0.77, with a TON value of 10040. This remarkable performance during the reaction can be attributed to the exceptional stability of the catalyst.

To identify the cause of the decrease in catalytic activity, ICP-OES analysis was carried out on the filtrates collected from the recycle runs (Fig. 5, dot and dashed line). The Ru content remaining in the recovered catalysts after each run was then estimated by subtracting the amount of leached Ru in the filtrate. For the Ru/MN-TiO₂ catalyst, the Ru content decreased from 1.35 wt% for the fresh catalyst to 0.93 wt% for the spent catalyst after the fifth recycle run, maintaining 68.9 % of the initial Ru content. In contrast, Ru/N-TiO₂ showed a more rapid decrease in the Ru content of the catalyst after the recycle tests, eventually reaching 0.45 wt%, equivalent to 36 % of its initial state. Ru/TiO₂ was found to be highly susceptible to leaching, as most of the Ru leached out even after the second run, indicating the crucial role of N-dopants in stabilizing the Ru species during hydrogenation. The calculated TON values based on the remaining Ru content of Ru/MN-TiO₂ were found to be similar and well-maintained during the recycling tests, with a slight decrease of less

than 10 % in the initial TON until the third recycling run. In contrast, the TON values for Ru/N-TiO₂ gradually decreased, while those for Ru/TiO₂ dropped rapidly (Table S4).

To trace the chemical changes in the supported Ru species after the recycle tests, XPS analysis of the spent catalyst was conducted. Unfortunately, severe Ru leaching during the recycle tests, which was confirmed for the Ru/TiO₂ catalyst, led to its exclusion from further characterization. Fig. 6a presents deconvoluted Ru 3d XPS spectra for both Ru/MN-TiO₂ and Ru/N-TiO₂, indicating that the binding energy of Ru 3d_{5/2} was approximately 281.3 eV, thus implying that the oxidation state of the supported Ru species remained at 3⁺ after the reaction. Moreover, Cl 2p XPS spectra as shown in Fig. 6b exhibited a significant decrease in intensity after hydrogenation, likely due to the removal of Cl ligands during the reaction. As shown in Fig. 6, the Ru K-edge XANES spectra were obtained to investigate the oxidation state of the supported Ru species in the spent Ru/MN-TiO₂ and Ru/N-TiO₂ catalysts. The results revealed that the energy absorption threshold of the spent catalysts remained similar to that of RuCl₃ xH₂O, indicating that the oxidation state of the supported Ru species was maintained. Furthermore, the EXAFS spectra in Fig. 6d revealed a marked decrease in the intensity of the Ru-Cl radial distance at 1.9 Å, suggesting the absence of Cl species after hydrogenation. These results were consistent with the XPS results reported above. Moreover, both spent catalysts exhibited a distinct Ru radial distance at 1.6 Å, corresponding to the Ru-N bond. Notably, the metallic Ru-Ru scattering peak was observed with a very low intensity at 2.3 Å, suggesting that the supported Ru species remained atomically dispersed after the reaction, with only partial agglomeration into Ru nanoparticles.

These findings indicate that the decrease in specific activity of Ru/MN-TiO₂ and Ru/N-TiO₂ during the recycling tests is primarily due to the leaching of Ru. Specifically, the results suggest that the stability of

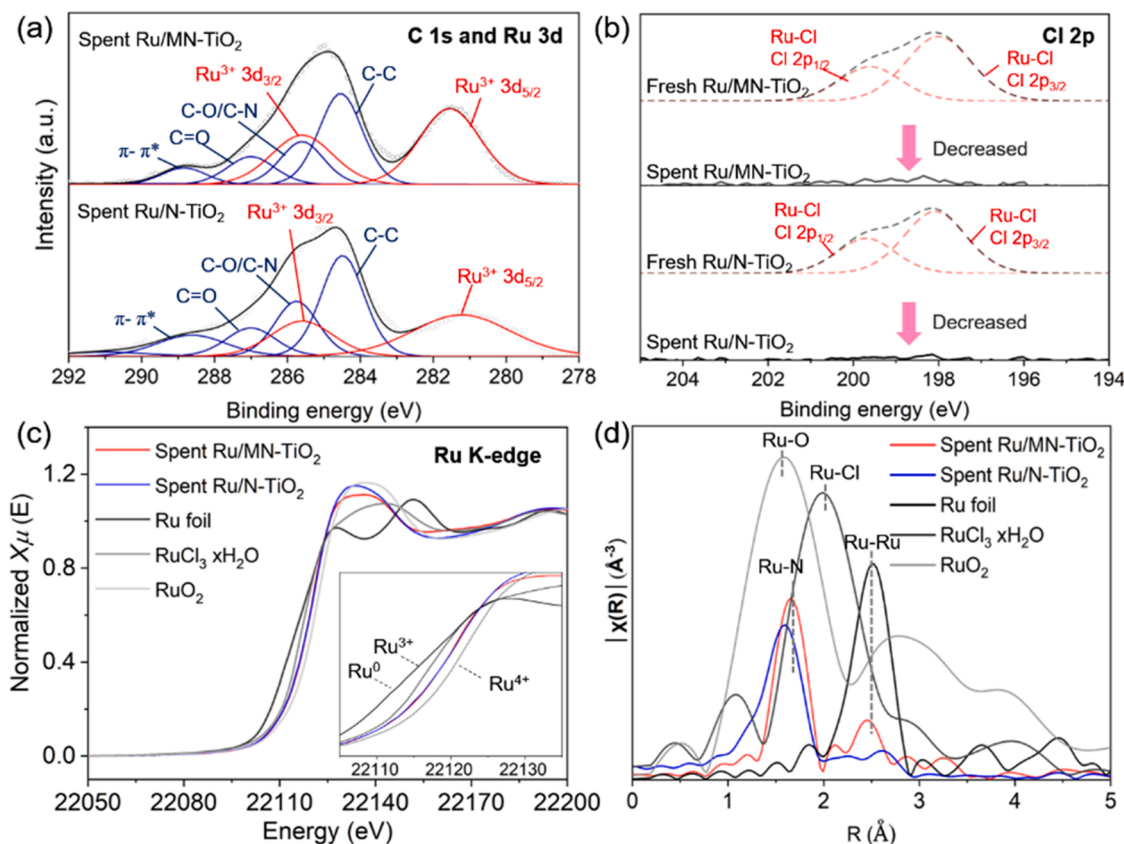


Fig. 6. Characterization of spent catalysts. Deconvoluted (a) C 1s and Ru 3d XPS spectra and (b) Cl 2p spectra for spent Ru/MN-TiO₂ and Ru/N-TiO₂. (c) Ru K-edge X-ray absorption near-edge structure and (d) Extended X-ray absorption fine structure spectra of spent Ru/MN-TiO₂ and Ru/N-TiO₂.

Ru/MN-TiO₂ against Ru leaching is higher than that of Ru/N-TiO₂ and Ru/TiO₂, which suggests that the coordination strength of Ru–Ns is stronger than that of Ru–Ni and Ru–O or Ru–Ti in the catalysts. Consequently, Ru single-atom catalysts supported on MN-TiO₂ can maintain an atomically dispersed state with exceptional stability under hydrogenation conditions. These results highlight the need for further investigation into the role of the Ti–N moiety to better understand the effects of various Ti–N structures on the Ru SAC.

3.4. Theoretical explanation of Ru single atom catalysts supported on the pristine and N-doped TiO₂

A theoretical investigation was conducted using DFT calculations to validate the influence of N-dopants on the structural properties of the Ru SACs. The bare anatase (101) plane and N-doped anatase (101) plane in the interstitial and substitutional sites with a four-layer structure were used to simulate the adsorption behavior of RuCl₃ and was named TiO₂, N_i-TiO₂, and N_s-TiO₂, respectively. As shown in Fig. 7a, the optimized

catalyst structure of RuCl₃/TiO₂ shows that RuCl₃ is adsorbed and forms a bond between Ru and the exposed O sites on the (101) TiO₂ surface. In contrast, the optimal structural models for RuCl₃ supported on N-TiO₂ show that the Ru species are adsorbed to N-dopant sites, resulting in bonds with Ru–N_i and Ru–O for RuCl₃/N_i-TiO₂ and Ru–N_s and Ru–O for RuCl₃/N_s-TiO₂ (Fig. 7b and c). The optimized adsorption energies of the Ru chloride on each support surface are calculated to be –1.85 eV for RuCl₃/TiO₂, –3.44 eV for RuCl₃/N_i-TiO₂, and –4.15 eV for RuCl₃/N_s-TiO₂ (Fig. 7d). These results indicate that the binding strength of Ru–N_s is stronger than those of Ru–N_i and Ru–O on the bare surface of the TiO₂ structure, which explains the enhanced catalytic stability of the Ru components on Ru/MN-TiO₂ against metal leaching and agglomeration during the reaction.

Furthermore, the electronic properties of Ru SACs supported on bare and two types of N-TiO₂ surfaces were investigated by DFT analyses. The partial density of the state diagram at the heterojunction between the supported Ru atom and each TiO₂ surface is presented in Fig. 7e and f [59–62]. At the bare anatase surface, the Fermi level of the

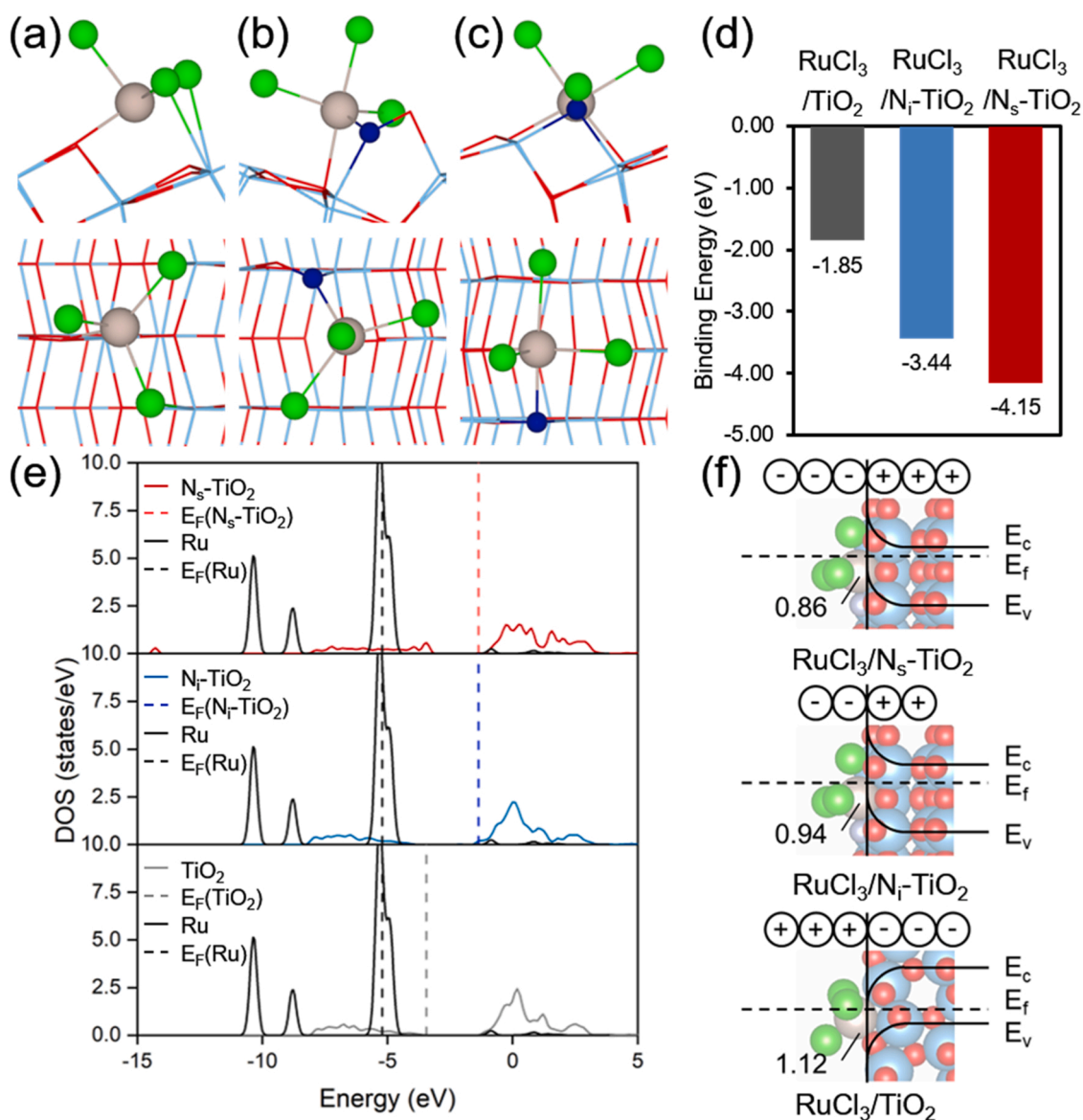


Fig. 7. (a–c) Side view (top) and top view (bottom) of optimized RuCl₃/TiO₂, RuCl₃/N_i-TiO₂, and RuCl₃/N_s-TiO₂ structures. Ti, O, N, Ru, and Cl atoms are expressed in pale blue, red, dark blue, gray, and green, respectively. (d) Binding energy of Ru species on each support structure. (e) Partial density of state diagram of Ru 4d and Ti 3d in RuCl₃/TiO₂, RuCl₃/N_i-TiO₂, and RuCl₃/N_s-TiO₂. (f) Schematic illustration of band bending, Bader charge of Ru (indicated number), and charge variation in RuCl₃/TiO₂, RuCl₃/N_i-TiO₂, and RuCl₃/N_s-TiO₂.

semiconductor (-3.450 eV) is placed above the valence band of the TiO_2 and is higher than Ru (-5.207 eV). This means that electrons move from the metal to the semiconductor and that the band bending can be deformed like a p-type junction. In contrast, when N is doped at the interstitial and substitutional sites of the anatase structure, the Fermi levels of the $\text{N}_i\text{-TiO}_2$ and $\text{N}_s\text{-TiO}_2$ surfaces increase to -1.359 and -1.357 eV, respectively, and are placed under the conduction band. This modified Fermi level induces a Schottky barrier in the n-type junction. Electrons move from the support to the metal atom and the charge on the Ru atom can change more negatively than the charge on the bare anatase surface. According to the Bader charge analysis in Table S5, the variation in the charge at the Ru single-atom is consistent. The Bader charge of the Ru atom on the N-TiO_2 changes from 1.12 to 0.94 and 0.86, which means that Ru can become more negative owing to the doping of N. This indicates that the electronic interaction between the Ru atom and $\text{N}_s\text{-TiO}_2$ can be more enhanced than the interaction between the Ru and $\text{N}_i\text{-TiO}_2$ or TiO_2 . It is also highly probable that the strong interaction between Ru and $\text{N}_s\text{-TiO}_2$ is the origin of the promoted adsorption strength of the Ru catalyst on MN-TiO_2 .

4. Conclusion

In summary, a N-TiO_2 support was prepared via calcination using mixed powder of melamine and Ti(OH)_4 under thermal conditions, which allowed the simultaneous growth of the TiO_2 structure and the N-doping process. From the analyses and catalytic activity tests, MN-TiO_2 was chosen as the optimal catalyst support among the pristine TiO_2 and N-doped TiO_2 synthesized by using conventional method for the hydrogenation of CO_2 to FA. It possessed the abundant polycrystalline structure of TiN and TiO_2 and the dominant presence of electron-rich N-dopant sites with two types of chemical states, namely N_s and N_i sites. The stable and isolated Ru dispersion state coordinated to N-dopant sites on Ru/MN-TiO_2 was characterized by evident changes in the electronic properties of the N atoms in the TiO_2 lattice structure. The improved recyclability of Ru/MN-TiO_2 was observed in successive batch runs of the CO_2 hydrogenation to formate, retaining 42 % of its original relative activity after the fifth recycle test. However, Ru/N-TiO_2 , which was analyzed to contain only N_i -dopant sites, registered a lower stability, retaining 19 % of initial specific activity after the fifth run. Meanwhile, Ru/TiO_2 was completely deactivated by the third run, revealing the significant role of the N-dopants in the TiO_2 structure in improving the stability of the catalytic Ru species during hydrogenation. The effect of the N-dopants on the immobilized Ru atoms was validated using DFT calculations. These demonstrated the stronger binding ability of the N_s sites to the Ru species than the N_i sites and the bare surface of the TiO_2 structure, which enabled the Ru components to be more durable against metal leaching and agglomeration. This study revealed the underlying role played by electron-donating dopants on the TiO_2 support for the stabilization of supported metals under thermal and reductive conditions, suggesting a promising avenue for designing a highly stable catalyst for various chemical transformations by a simple approach using metal oxide supports.

CRediT authorship contribution statement

K. Park: Conceptualization, Investigation, Writing – original draft, Writing – review & editing. **K.R. Lee:** Conceptualization, Investigation, Writing – original draft, Writing – review & editing. **S. Ahn:** Investigation, Validation. **S.-H. Kim:** Investigation, Validation. **A. Haider:** Investigation. **S. Choung:** Formal analysis. **J.W. Han:** Formal analysis. **K.-D. Jung:** Supervision, Resources, Writing – review & editing, Project administration, Funding acquisition.

Declaration of Competing Interest

The authors declare that they have no known competing financial

interests or personal relationships that could have appeared to influence the work reported in this paper.

Data Availability

Data will be made available on request.

Acknowledgments

This work was supported by the Korea Institute of Science and Technology (KIST) and the Carbon to X Project (2020M3H7A1096360) through the National Research Foundation (NRF) (Ministry of Science ICT & Future Planning). X-ray absorption spectroscopy study was supported by the 8C, 10C and 10D beamline of the Pohang Accelerator Laboratory (Republic of Korea) under contact no. 2023–1st-8C-078 and 2023–1st-10C-087. Theoretical investigation with DFT calculation was supported by Density Functional Calculation was supported by the National Supercomputing Center with supercomputing resources including technical support (KSC-2021-CRE-0543).

Appendix A. Supporting information

Supplementary data associated with this article can be found in the online version at [doi:10.1016/j.apcatb.2023.122873](https://doi.org/10.1016/j.apcatb.2023.122873).

References

- [1] D. Teichmann, W. Arlt, P. Wasserscheid, R. Freymann, A future energy supply based on Liquid Organic Hydrogen Carriers (LOHC), *Energy Environ. Sci.* 4 (2011) 2767–2773, <https://doi.org/10.1039/C1EE01454D>.
- [2] D. Geburtig, P. Preuster, A. Bösmann, K. Müller, P. Wasserscheid, Chemical utilization of hydrogen from fluctuating energy sources–Catalytic transfer hydrogenation from charged Liquid Organic Hydrogen Carrier systems, *Int. J. Hydrogen Energy* 41 (2016) 1010–1017, <https://doi.org/10.1016/j.ijhydene.2015.10.013>.
- [3] P. Preuster, C. Papp, P. Wasserscheid, Liquid organic hydrogen carriers (LOHCs): toward a hydrogen-free hydrogen economy, *Acc. Chem. Res.* 50 (2017) 74–85, <https://doi.org/10.1021/acs.accounts.6b00474>.
- [4] P.T. Aakko-Saksa, C. Cook, J. Kiviahio, T. Repo, Liquid organic hydrogen carriers for transportation and storing of renewable energy–Review and discussion, *J. Power Sources* 396 (2018) 803–823, <https://doi.org/10.1016/j.jpowsour.2018.04.011>.
- [5] M. Grasemann, G. Laurenczy, Formic acid as a hydrogen source–Recent developments and future trends, *Energy Environ. Sci.* 5 (2012) 8171–8181, <https://doi.org/10.1039/C2EE21928J>.
- [6] D. Mellmann, P. Sponholz, H. Junge, M. Beller, Formic acid as a hydrogen storage material–development of homogeneous catalysts for selective hydrogen release, *Chem. Soc. Rev.* 45 (2016) 3954–3988, <https://doi.org/10.1039/C5CS00618J>.
- [7] T. Zell, R. Langer, CO_2 -based hydrogen storage–formic acid dehydrogenation, *Phys. Sci. Rev.* 3 (2018) 57–94, <https://doi.org/10.1515/psr-2017-0012>.
- [8] L. Zhang, W. Wu, Z. Jiang, T. Fang, A review on liquid-phase heterogeneous dehydrogenation of formic acid: recent advances and perspectives, *Chem. Pap.* 72 (2018) 2121–2135, <https://doi.org/10.1007/s11696-018-0469-8>.
- [9] T. Schaub, R.A. Paciello, A process for the synthesis of formic acid by CO_2 hydrogenation: thermodynamic aspects and the role of CO, *Angew. Chem. Int. Ed.* 50 (2011) 7278–7282, <https://doi.org/10.1002/anie.201101292>.
- [10] T. Schaub, D.M. Fries, R. Paciello, K.-D. Mohl, M. Schäfer, S. Rittinger, D. Schneider, Process for preparing formic acid by reaction of carbon dioxide with hydrogen, U.S. Patent, 2014, NO. 8,791,297.
- [11] Y. Wang, D. He, H. Chen, D. Wang, Catalysts in electro-, photo- and photoelectrocatalytic CO_2 reduction reactions, *J. Photochem. Photobiol. C: Photochem. Rev.* 40 (2019) 117–149, <https://doi.org/10.1016/j.jphotochemrev.2019.02.002>.
- [12] Z. Sun, J. Dong, C. Chen, S. Zhang, Y. Zhu, Photocatalytic and electrocatalytic CO_2 conversion: from fundamental principles to design of catalysts, *J. Chem. Technol. Biotechnol.* 96 (2021) 1161–1175, <https://doi.org/10.1002/jctb.6653>.
- [13] W. Wang, Y. Himeda, J.T. Muckerman, G.F. Manbeck, E. Fujita, CO_2 hydrogenation to formate and methanol as an alternative to photo- and electrochemical CO_2 reduction, *Chem. Rev.* 115 (2015) 12936–12973, <https://doi.org/10.1021/acs.chemrev.5b00197>.
- [14] K. Sordakis, C. Tang, L.K. Vogt, H. Junge, P.J. Dyson, M. Beller, G. Laurenczy, Homogeneous catalysis for sustainable hydrogen storage in formic acid and alcohols, *Chem. Rev.* 118 (2018) 372–433, <https://doi.org/10.1021/acs.chemrev.7b00182>.
- [15] D.A. Bulushev, J.R. Ross, Heterogeneous catalysts for hydrogenation of CO_2 and bicarbonates to formic acid and formates, *Catal. Rev. Sci. Eng.* 60 (2018) 566–593, <https://doi.org/10.1080/01614940.2018.1476806>.

- [16] A. Álvarez, A. Bansode, A. Urakawa, A.V. Bavykina, T.A. Wezendonk, M. Makkee, J. Gascon, F. Kapteijn, Challenges in the greener production of formates/formic acid, methanol, and DME by heterogeneously catalyzed CO₂ hydrogenation processes, *Chem. Rev.* 117 (2017) 9804–9838, <https://doi.org/10.1021/acs.chemrev.6b00816>.
- [17] R. Sun, Y. Liao, S. Bai, M. Zheng, C. Zhou, T. Zhang, B.F. Sels, Heterogeneous catalysts for CO₂ hydrogenation to formic acid/formate: from nanoscale to single atom, *Energy Environ. Sci.* 14 (2021) 1247–1285, <https://doi.org/10.1039/D0EE03575K>.
- [18] A. Modak, A. Ghosh, A. Bhaumik, B. Chowdhury, CO₂ hydrogenation over functional nanoporous polymers and metal-organic frameworks, *Adv. Colloid Interface Sci.* 290 (2021), 102349, <https://doi.org/10.1016/j.cis.2020.102349>.
- [19] P. Verma, S. Zhang, S. Song, K. Mori, Y. Kuwahara, M. Wen, H. Yamashita, T. An, Recent strategies for enhancing the catalytic activity of CO₂ hydrogenation to formate/formic acid over Pd-based catalyst, *J. CO₂ Util.* 54 (2021), 101765, <https://doi.org/10.1016/j.jcou.2021.101765>.
- [20] G.H. Gunasekar, K. Park, K.-D. Jung, S. Yoon, Recent developments in the catalytic hydrogenation of CO₂ to formic acid/formate using heterogeneous catalysts, *Inorg. Chem. Front.* 3 (2016) 882–895, <https://doi.org/10.1039/C5QI00231A>.
- [21] R. Luo, W. Xu, M. Chen, X. Liu, Y. Fang, H. Ji, Covalent triazine frameworks obtained from nitrile monomers for sustainable CO₂ catalysis, *ChemSusChem* 13 (2020) 6509–6522, <https://doi.org/10.1002/cssc.202002422>.
- [22] G.H. Gunasekar, S. Yoon, New aspects of covalent triazine frameworks in heterogeneous catalysis, in: Samahe Sadjadi (Ed.), *Emerging Carbon Materials for Catalysis*, Elsevier, Amsterdam, 2021, pp. 1–32, <https://doi.org/10.1016/B978-0-12-817561-3.00001-9>.
- [23] K. Park, G.H. Gunasekar, S. Yoon, Heterogenized catalyst for the hydrogenation of CO₂ to formic acid or its derivatives, in: Yuichiro Himeda (Ed.), *CO₂ Hydrogenation Catalysis*, John Wiley & Sons, Hoboken, 2021, pp. 149–177, <https://doi.org/10.1002/9783527824113.ch6>.
- [24] M. Liu, Y. Xu, Y. Meng, L. Wang, H. Wang, Y. Huang, N. Onishi, L. Wang, Z. Fan, Y. Himeda, Heterogeneous catalysis for carbon dioxide mediated hydrogen storage technology based on formic acid, *Adv. Energy Mater.* 12 (2022), 2200817, <https://doi.org/10.1002/aenm.202200817>.
- [25] K. Mori, H. Yamashita, Design and architecture of nanostructured heterogeneous catalysts for CO₂ hydrogenation to formic acid/formate, in: Yuichiro Himeda (Ed.), *CO₂ Hydrogenation Catalysis*, John Wiley & Sons, Hoboken, 2021, pp. 179–205, <https://doi.org/10.1002/9783527824113.ch7>.
- [26] Z. Yang, H. Zhang, B. Yu, Y. Zhao, G. Ji, Z. Liu, A. Tröger's, base-derived microporous organic polymer: design and applications in CO₂/H₂ capture and hydrogenation of CO₂ to formic acid, *Chem. Commun.* 51 (2015) 1271–1274, <https://doi.org/10.1039/C4CC08295H>.
- [27] G.M. Eder, D.A. Pyles, E.R. Wolfson, P.L. McGrier, A ruthenium porphyrin-based porous organic polymer for the hydrosilylative reduction of CO₂ to formate, *Chem. Commun.* 55 (2019) 7195–7198, <https://doi.org/10.1039/C9CC02273B>.
- [28] B. Chen, M. Dong, S. Liu, Z. Xie, J. Yang, S. Li, Y. Wang, J. Du, H. Liu, B. Han, CO₂ Hydrogenation to Formate Catalyzed by Ru Coordinated with a N,P-Containing Polymer, *ACS Catal.* 10 (2020) 8557–8566, <https://doi.org/10.1021/acscatal.0c01678>.
- [29] A. Kann, H. Hartmann, A. Besmehn, P.J.C. Hausoul, R. Palkovits, Hydrogenation of CO₂ to Formate over Ruthenium Immobilized on Solid Molecular Phosphines, *ChemSusChem* 11 (2018) 1857–1865, <https://doi.org/10.1002/cssc.201800413>.
- [30] C. Wu, F. Irshad, M. Luo, Y. Zhao, X. Ma, S. Wang, Ruthenium complexes immobilized on an azolium based metal organic framework for highly efficient conversion of CO₂ into formic acid, *ChemCatChem* 11 (2019) 1256–1263, <https://doi.org/10.1002/cctc.201801701>.
- [31] Z. Li, T.M. Rayder, L. Luo, J.A. Byers, C.-K. Tsung, Aperture-opening encapsulation of a transition metal catalyst in a metal-organic framework for CO₂ hydrogenation, *J. Am. Chem. Soc.* 140 (2018) 8082–8085, <https://doi.org/10.1021/jacs.8b04047>.
- [32] K. Park, G.H. Gunasekar, N. Prakash, K.D. Jung, S. Yoon, A highly efficient heterogenized iridium complex for the catalytic hydrogenation of carbon dioxide to formate, *ChemSusChem* 8 (2015) 3410–3413, <https://doi.org/10.1002/cssc.201500436>.
- [33] G.H. Gunasekar, J. Shin, K. Jung, K. Park, S. Yoon, Design strategy toward recyclable and highly efficient heterogeneous catalysts for the hydrogenation of CO₂ to formate, *ACS Catal.* 8 (2018) 4346–4353, <https://doi.org/10.1021/acscatal.8b00392>.
- [34] K. Park, G.H. Gunasekar, S. Kim, H. Park, S. Kim, K. Park, K. Jung, S. Yoon, CO₂ hydrogenation to formic acid over heterogenized ruthenium catalysts using a fixed bed reactor with separation units, *Green Chem.* 22 (2020) 1639–1649, <https://doi.org/10.1039/C9GC03685G>.
- [35] S. Ahn, K. Park, K.R. Lee, A. Haider, C. Van Nguyen, H. Jin, S.J. Yoo, S. Yoon, K. Jung, Atomically dispersed Ru (III) on N-doped mesoporous carbon hollow spheres as catalysts for CO₂ hydrogenation to formate, *Chem. Eng. J.* 442 (2022), 136185, <https://doi.org/10.1016/j.cej.2022.136185>.
- [36] A. Jaleel, A. Haider, C. Van Nguyen, K.R. Lee, S. Choung, J.W. Han, S. Baek, C. Shin, K. Jung, Structural effect of nitrogen/carbon on the stability of anchored Ru catalysts for CO₂ hydrogenation to formate, *Chem. Eng. J.* 433 (2022), 133571, <https://doi.org/10.1016/j.cej.2021.133571>.
- [37] Z. Xu, N.D. McNamara, G.T. Neumann, W.F. Schneider, J.C. Hicks, Catalytic hydrogenation of CO₂ to formic acid with silica-tethered iridium catalysts, *ChemCatChem* 5 (2013) 1769–1771, <https://doi.org/10.1002/cctc.201200839>.
- [38] H.K. Lo, C. Copéret, CO₂ hydrogenation to formate with immobilized Ru-catalysts based on hybrid organo-silica mesostructured materials, *ChemCatChem* 11 (2019) 430–434, <https://doi.org/10.1002/cctc.201801368>.
- [39] R. Asahi, T. Morikawa, H. Irie, T. Ohwaki, Nitrogen-doped titanium dioxide as visible-light-sensitive photocatalyst: designs, developments, and prospects, *Chem. Rev.* 114 (2014) 9824–9852, <https://doi.org/10.1021/cr5000738>.
- [40] X. Chen, A. Selloni, Introduction: Titanium dioxide (TiO₂) nanomaterials, *Chem. Rev.* 114 (2014) 9281–9282, <https://doi.org/10.1021/cr500422r>.
- [41] S.A. Ansari, M.M. Khan, M.O. Ansari, M.H. Cho, Nitrogen-doped titanium dioxide (N-doped TiO₂) for visible light photocatalysis, *New J. Chem.* 40 (2016) 3000–3009, <https://doi.org/10.1039/C5NJ03478G>.
- [42] T. Morikawa, T. Ohwaki, K. Suzuki, S. Moribe, S. Tero-Kubota, Visible-light-induced photocatalytic oxidation of carboxylic acids and aldehydes over N-doped TiO₂ loaded with Fe, Cu or Pt, *Appl. Catal. B-Environ.* 83 (2008) 56–62, <https://doi.org/10.1016/j.apcatb.2008.01.034>.
- [43] D. Tan, J. Zhang, J. Shi, S. Li, B. Zhang, X. Tan, F. Zhang, L. Liu, D. Shao, B. Han, Photocatalytic CO₂ transformation to CH₄ by Ag/Pd bimetal supported on N-doped TiO₂ nanosheet, *ACS Appl. Mater. Interfaces* 10 (2018) 24516–24522, <https://doi.org/10.1021/acsami.8b06320>.
- [44] C. Ao, P. Tian, L. Ouyang, G. Da, X. Xu, J. Xu, Y. Han, Dispersing Pd nanoparticles on N-doped TiO₂: a highly selective catalyst for H₂O₂ synthesis, *Catal. Sci. Technol.* 6 (2016) 5060–5068, <https://doi.org/10.1039/C5CY02275D>.
- [45] P. Chen, A. Khetan, F. Yang, V. Migunov, P. Weide, S.P. Stürmer, P. Guo, K. Kähler, W. Xia, J. Mayer, Experimental and theoretical understanding of nitrogen-doping-induced strong metal-support interactions in Pd/TiO₂ catalysts for nitrobenzene hydrogenation, *ACS Catal.* 7 (2017) 1197–1206, <https://doi.org/10.1021/acscatal.6b02963>.
- [46] B. Yan, D. Liu, X. Feng, M. Shao, Y. Zhang, Ru species supported on MOF-derived N-doped TiO₂/C hybrids as efficient electrocatalytic/photocatalytic hydrogen evolution reaction catalysts, *Adv. Funct. Mater.* 30 (2020), 2003007, <https://doi.org/10.1002/adfm.202003007>.
- [47] Q. Yu, Q. Xu, H. Li, K. Yang, X. Li, Effects of heat treatment on the structure and photocatalytic activity of polymer carbon nitride, *J. Mater. Sci.* 54 (2019) 14599–14608, <https://doi.org/10.1007/s10853-019-03895-w>.
- [48] Z. Zhang, X. Wang, J. Long, Q. Gu, Z. Ding, X. Fu, Nitrogen-doped titanium dioxide visible light photocatalyst: spectroscopic identification of photoactive centers, *J. Catal.* 276 (2010) 201–214, <https://doi.org/10.1016/j.jcat.2010.07.033>.
- [49] J. Lynch, C. Giannini, J.K. Cooper, A. Loudice, I.D. Sharp, R. Buonsanti, Substitutional or interstitial site-selective nitrogen doping in TiO₂ nanostructures, *J. Phys. Chem. C* 119 (2015) 7443–7452, <https://doi.org/10.1021/jp512775s>.
- [50] L. Soriano, M. Abbate, J. Fuggle, P. Prieto, C. Jiménez, J. Sanz, L. Galán, S. Hofmann, Thermal oxidation of TiN studied by means of soft x-ray absorption spectroscopy, *J. Vac. Sci. Technol. A- Vac. Surf. Films* 11 (1993) 47–51, <https://doi.org/10.1116/1.578718>.
- [51] H. Chen, A. Nambu, W. Wen, J. Graciani, Z. Zhong, J.C. Hanson, E. Fujita, J. A. Rodriguez, Reaction of NH₃ with titania: N-doping of the oxide and TiN formation, *J. Phys. Chem. C* 111 (2007) 1366–1372, <https://doi.org/10.1021/jp066137e>.
- [52] A. Braun, K.K. Akurati, G. Fortunato, F.A. Reifler, A. Ritter, A.S. Harvey, A. Vital, T. Graule, Nitrogen doping of TiO₂ photocatalyst forms a second eg state in the oxygen 1s NEXAFS pre-edge, *J. Phys. Chem. C* 114 (2010) 516–519, <https://doi.org/10.1021/jp908875t>.
- [53] D.K. Lee, J.I. Choi, G.H. Lee, Y.H. Kim, J.K. Kang, Energy states of a core-shell metal oxide photocatalyst enabling visible light absorption and utilization in solar-to-fuel conversion of carbon dioxide, *Adv. Energy Mater.* 6 (2016), 1600583, <https://doi.org/10.1002/aenm.201600583>.
- [54] D. Wang, L. Liu, X. Sun, T. Sham, Observation of lithiation-induced structural variations in TiO₂ nanotube arrays by X-ray absorption fine structure, *J. Mater. Chem. A* 3 (2015) 412–419, <https://doi.org/10.1039/C4TA04873C>.
- [55] D.J. Morgan, Resolving ruthenium: XPS studies of common ruthenium materials, *Surf. Interface Anal.* 47 (2015) 1072–1079, <https://doi.org/10.1002/sia.5852>.
- [56] S. Eckle, H. Anfang, R.J. Behm, Reaction intermediates and side products in the methanation of CO and CO₂ over supported Ru catalysts in H₂-rich reformate gases, *J. Phys. Chem. C* 115 (2011) 1361–1367, <https://doi.org/10.1021/jp108106t>.
- [57] H.V. Thang, S. Tosoni, L. Fang, P. Bruijninx, G. Pacchioni, Nature of sintering-resistant, single-atom Ru species dispersed on zirconia-based catalysts: A DFT and FTIR study of CO adsorption, *ChemCatChem* 10 (2018) 2634–2645, <https://doi.org/10.1002/cctc.201800246>.
- [58] S. Xu, S. Chansai, S. Xu, C.E. Stere, Y. Jiao, S. Yang, C. Hardacre, X. Fan, CO poisoning of Ru catalysts in CO₂ hydrogenation under thermal and plasma conditions: a combined kinetic and diffuse reflectance infrared fourier transform spectroscopy-mass spectrometry study, *ACS Catal.* 10 (2020) 12828–12840, <https://doi.org/10.1021/acscatal.0c03620>.
- [59] Z.H. Xue, J.T. Han, W.J. Feng, Q.Y. Yu, X.H. Li, M. Antonietti, J.S. Chen, Tuning the adsorption energy of methanol molecules along Ni-N-doped carbon phase boundaries by the Mott-Schottky effect for gas-phase methanol dehydrogenation, *Angew. Chem.* 130 (2018) 2727–2731, <https://doi.org/10.1002/ange.201713429>.
- [60] S. Cheng, X. Meng, N. Shang, S. Gao, C. Feng, C. Wang, Z. Wang, Pd supported on g-C₃N₄ nanosheets: Mott-Schottky heterojunction catalyst for transfer hydrogenation of nitroarenes using formic acid as hydrogen source, *New J. Chem.* 42 (2018) 1771–1778, <https://doi.org/10.1039/C7NJ04268J>.
- [61] T. He, G. Kour, X. Mao, A. Du, Cu⁺ active sites stabilization through Mott-Schottky effect for promoting highly efficient conversion of carbon monoxide into n-propanol, *J. Catal.* 382 (2020) 49–56, <https://doi.org/10.1016/j.jcat.2019.12.015>.
- [62] Q. Wei, J. Wang, W. Shen, Atomically dispersed Fe³⁺ anchored on nitrogen-rich carbon for enhancing benzyl alcohol oxidation through Mott-Schottky effect, *Appl. Catal. B-Environ.* 292 (2021), 120195, <https://doi.org/10.1016/j.apcatb.2021.120195>.